Energy Storage Materials 80 (2025) 104374

Contents lists available at ScienceDirect

Energy Storage Materials

journal homepage: www.elsevier.com/locate/ensm

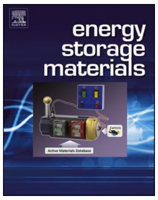

A dilute and non-flammable electrolyte engineering enables stable SEI for low-temperature zinc batteries

Rujian Fu [a,#], Bo Zhang [a,#], Tiantian Lu [a], Chang Liu [a], Lifeng Hou [a], Shi Wang [b,*], Yihang Ning [c], Zhong Jin [d,*], Qian Wang [a,*]

[a] College of Materials Science and Engineering, Taiyuan University of Technology, Taiyuan 030024, Shanxi, China
[b] State Key Laboratory of Flexible Electronics (LoFE) & Institute of Advanced Materials (IAM), Nanjing University of Posts & Telecommunications, Nanjing 210023, China
[c] China State Shipbuilding Corporation Haizhuang Wind Power Co., Ltd, Chongqing 401120, China
[d] School of Chemistry & Chemical Engineering, Nanjing University, Nanjing 210023, China

ARTICLE INFO

Keywords:
Zn metal anode
Zn-ion batteries
Dilute electrolyte
SEI layer
ZnF_2

ABSTRACT

Zn-ion batteries (ZIBs) have garnered significant attention due to their environmental friendliness and low cost. However, severe dendritic Zn growth, surface corrosion, and H_2 evolution reactions, have limited their further application. In this work, we construct a dilute and non-flammable electrolyte composed of 0.5 M $Zn(BF_4)_2$ salts in a cosolvent of tetrahydrofuran (THF)/triethyl phosphate (TEP) (1:2 by volume) for ZIBs. In such an electrolyte, the use of co-solvents can reduce the freezing point of electrolytes, thereby guaranteeing high ionic conductivity and fluidity of electrolytes even at low temperatures. Meanwhile, TEP and THF can jointly participate in the Zn^{2+} solvation structure, forming a unique Zn^{2+} solvation sheath, $Zn(TEP)_{2.23}(THF)_{0.64}(H_2O)_{1.32}(BF_4)_{2.15}$, thus deriving a stable solid electrolyte interface (SEI) enriched with ZnF_2 and $Zn_3(PO_4)_2$ on the surface of Zn metal anode during electrochemical cycling to achieve high interfacial stability and rapid Zn^{2+} transport, especially at low temperatures. Thus, even at −20 °C, the Zn metal anode can maintain a high coulombic efficiency of 99.86 % over 1500 cycles in half cells, and exhibit a an extraordinarily long cycling life (>5000 h) in symmetric cells. Even under −40 °C, the symmetric cells can also run stably over 5000 h with low overpotential. And corresponding full cells also demonstrate high discharge capacity and capacity retention. This work offers a basic reference for designing safe and low-cost electrolytes towards low-temperature ZIBs.

1. Introduction

Zn metal anode has a theoretical capacity of 820 mAh g^{-1} and a volumetric capacity of 5855 mAh cm^{-3}, coupled with its abundant reserves and low cost, making ZIBs a promising candidate for next-generation energy storage systems [1–5] Meanwhile, typical aqueous electrolytes stand out for their environmental sustainability, high safety, and superior ionic conductivity [6–8] Nevertheless, the unstable anode/electrolyte interface significantly hinders the practical application of aqueous ZIBs, especially at low temperatures [9–11] For a conventional aqueous electrolyte, the interface usually faces several significant challenges, such as: H_2 evolution reaction (HER), dendrite growth, surface corrosion, etc., causing by the heightened reactivity of H_2O molecules and the weak acidity of electrolyte, culminating in poor coulombic efficiency (CE) and electrode utilization rates [12–15] Moreover, when the temperature drops below 0 °C, the hydrogen bonding interactions between H_2O molecules are enhanced, leading to the gradual solidification of aqueous electrolyte, which increases the interfacial impedance and slows down the Zn^{2+} diffusion kinetics, as well as increases the de-solvation energy, ultimately exacerbating interfacial side reactions and affecting the electrochemical performance of ZIBs [16–19] Thus, there is an urgent need to stabilize the interface for promoting the practical application of ZIBs.

Electrolyte design stands out as the most direct strategy to stabilize the Zn anode interface and enhance the low-temperature performance of ZIBs. It mainly focuses on the following aspects: 1) introducing electrolyte additives to participate in Zn^{2+} solvation sheath and regulate SEI formation; [20–23] 2) improving Zn salts concentration to reduce free

---

[*] Corresponding authors.
E-mail addresses: iamshiwang@njupt.edu.cn (S. Wang), zhongjin@nju.edu.cn (Z. Jin), qianwang0825@pku.edu.cn (Q. Wang).
[#] Authors equally contributed to this work.

https://doi.org/10.1016/j.ensm.2025.104374
Received 16 April 2025; Received in revised form 25 May 2025; Accepted 2 June 2025

H_2O molecules [24–27]; 3) introducing organic solvents as co-solvents to regulate the hydrogen bonding between H_2O molecules, reducing the freezing point of electrolytes and the number of reactive H_2O molecules [28–31] However, although introducing electrolyte additives and improving Zn salts concentration can regulate the Zn^{2+} solvation sheath and optimize the SEI film composition to a certain extent, their efficacy is impeded at low temperatures due to electrolyte solidification and Zn salt precipitation, posing significant challenges [32–35] By comparison, introducing organic solvents as co-solvents or even directly using organic solvents can significantly lower the freezing point of the electrolyte, thereby enabling their effectiveness at low temperatures, which have been conceptually, but not sufficiently, reported by a few groups. For instance, Han et al. reported a hydrated organic electrolyte, composed of 4 M $Zn(BF_4)_2$ and ethylene glycol, which can form ZnF_2-rich SEI film and ensure the run of ZIBs at −30 °C [36] Similarly, Wang Group designed a eutectic electrolyte composed of 4 M $Zn(BF_4)_2$ and 1,2-Dimethoxyethane (DME) [37] These works showcase great potential of organic electrolyte design and offer another avenue for constructing stable interface. Nonetheless, there is still much ground to cover, such as:the cost and pH issues of electrolyte caused by high Zn $(BF_4)_2$ concentration, safety issues caused by organic solvent. It is particularly noteworthy that these studies primarily employ high-concentration salts to construct an anion-dominated solvation structure. Recently, our Group demonstrated a thin and homogeneous SEI enriched with ZnF_2 and ZnS on Zn metal surface by a dilute electrolyte system composed of 1 M $Zn(BF_4)_2$ salt with dimethyl sulfoxide (DMSO) [38] Although the concentration of Zn salts has been reduced to 1 M, there are still safety hazards.

Here, we developed a low-concentration and non-flammable electrolyte, which was composed of 0.5 M $Zn(BF_4)_2$ salts in a co-solvent of THF/TEP (1:2 by volume). Highly flame-retardant TEP not only enhances the safety of the electrolyte, but also participates in the Zn^{2+} solvation sheath, consequently facilitating the formation of stable SEI layer. Thus, the obtained electrolyte displayed high safety and low-temperature tolerance. Meanwhile, it can also help to form a unique anion-enriched Zn^{2+}-solvation sheath, characterized as $Zn(TEP)_{2.23}(THF)_{0.64}(H_2O)_{1.32}(BF_4)_{2.15}$, leading to the formation of a stable SEI layer enriched with ZnF_2 and $Zn_3(PO_4)_2$ during cycling, which suppresses interface side reactions and endows rapid Zn^{2+} transport kinetics, especially at low-temperature. Consequently, at room temperature, the Zn || Zn symmetric cells can stably cycle for over 3000 h at a current density of 1 mA cm^{-2}, and Zn | Cu half cells can maintain a high CE of 99.82 % over 1500 cycles. It is worth noting that at −20 °C, Zn metal anode can also deliver a long cycling life in symmetric cells (>5000 h) and half cells (> 2500 cycles). Even at −40 °C, the symmetric cells can still stably cycle for over 5000 h. This work provides a feasible strategy for constructing safe organic electrolytes.

2. Result and discussion

2.1. *Electrolyte optimization and structure*

It is well-established that electrolyte composition and interfacial stability are critically interdependent in electrochemical systems. In ZIBs, electrolyte decomposition governs the SEI formation, where the strategic selection of Zn salts, solvents, and their synergistic interactions during SEI formation directly dictates battery performance. Recently, a Zn salt rich in F elements, $Zn(BF_4)_2$, has been developed and attempted in ZIBs because it has low cost and can promote the formation of a ZnF_2-enriched SEI layer. However, aqueous solutions of $Zn(BF_4)_2$ exhibit extreme acidity (pH<1 at 2.0 M), which leads to serious hydrogen evolution reactions and surface corrosion. Using organic solvents instead of H_2O is an effective strategy, but this in turn greatly reduces the safety of the electrolyte. Based on this, we constructed a dilute and non-flammable electrolyte, consisting of 0.5 M $Zn(BF_4)_2$ and THF/TEP co-solvents. As shown in Fig. 1, THF with low freezing point and viscosity can ensure good fluidity of the electrolyte even at low temperatures, while highly flame-retardant TEP can enhance the safety of the electrolyte. Meanwhile, introducing THF, with a low dielectric constant, into TEP can enhance the interaction between Zn^{2+} and BF_4^- (Table S1). Ultimately, a unique Zn^{2+} solvation sheath where THF and TEP participate together can be formed in such an electrolyte, thereby deriving a SEI enriched with ZnF_2 and $Zn_3(PO_4)_2$ on the Zn metal surface during the charging and discharging cycle. Such a SEI layer can not only

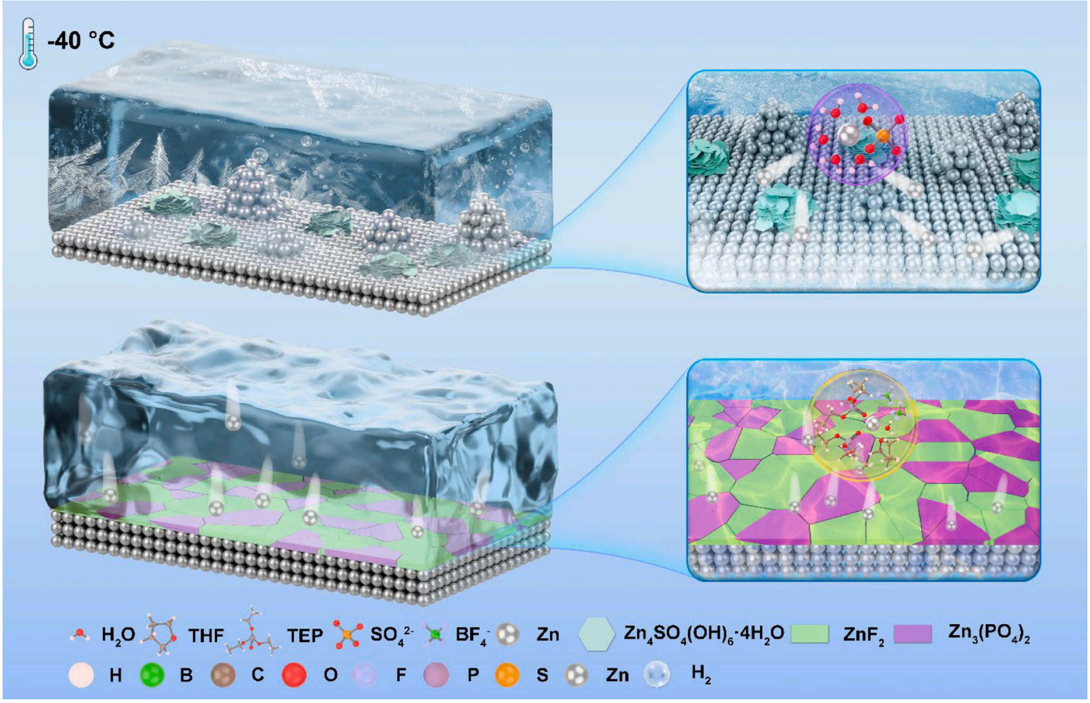

Fig. 1. Schematic illustration of solvation structures and electrode-electrolyte interfaces for different electrolytes.

suppress interface side reactions, but also can promote rapid Zn^{2+} transport through SEI layer, ensuring stable electrochemical performance at low temperatures.

Subsequently, we have preliminarily optimized the ratio of TEP to THF based on safety testing. As shown in Fig. 2a and Figure S1, the concentration of $Zn(BF_4)_2$ was fixed at 0.5 M, the electrolytes featuring different volume ratios of THF to TEP (1:0, 2:1, 1:1, 1:2, and 0:1) were denoted as TEP-0, TEP-1, TEP-2, TEP-3, and TEP-4, respectively. In other words, TEP-0 and TEP-4 represent pure 0.5 M THF-based electrolyte and pure 0.5 M TEP-based electrolyte, respectively. When the THF: TEP ratio was 1:2, the electrolyte exhibited high flame retardancy. Meanwhile, the TEP-3 electrolyte displayed the highest coulomb efficiency (CE) and more negative hydrogen evolution potential, thus was selected as the optimized concentration (Figure S2 and Table S2). Notably, although the increase in the proportion of TEP in the electrolyte leads to an increase in ion conductivity especially at low temperature, safety is paramount for the practical application of ZIBs. After a holistic evaluation, the TEP-3 electrolyte was ultimately selected as the experimental group (Figure S3). Furthermore, as a consequence of the low pH ($pH<2$) of 0.5 M $Zn(BF_4)_2$ aqueous electrolyte, intensifying the HER, and corresponding cells failed after undergoing cycling for a mere 80 h at 1 mA cm^{-2} and 1 mAh cm^{-2} (Figure S4). Meanwhile, the corresponding electrochemical tests and optical images after immersion also demonstrated that the 0.5 M $Zn(BF_4)_2$ aqueous electrolyte caused severe Zn corrosion, rendering it practically useless (Figure S5). Therefore, in this work, a common 2.0 M $ZnSO_4{\cdot}7H_2O$ aqueous electrolyte was used as an experimental control group, named as: ZSO electrolyte.

Then, we conducted a detailed analysis of the physicochemical properties and structure of the TEP-3 electrolyte. As shown in Figure S6, optical photographs revealed that TEP-3 electrolyte can maintain a fluidic state throughout the temperature range (−40 °C to 25 °C), contrasting with the solidification of ZSO electrolyte at −20 °C. Furthermore, the freezing point (T_f) of TEP-3 electrolyte was investigated by differential scanning calorimetry (DSC). As shown in Fig. 2b, when the temperature was increased from −170 °C to 25 °C, TEP-3 electrolyte did not exhibit a significant enthalpy change peak, which can be attributed to its glassy state at low temperatures, characterized by a glass transition temperature (T_g) of −137.64 °C. By comparison, ZSO electrolyte showed an obvious enthalpy change peak, corresponding a T_f of −11.42 °C. The freezing point of the pure 0.5 M $Zn(BF_4)_2$ aqueous electrolyte was also tested. Due to the low concentration, the electrolyte exhibited a higher freezing point compared to the ZSO electrolyte (Figure S7). In addition, interface wettability is also a key physicochemical indicator for electrolytes. As shown in Figure S8, the contact angle between TEP-3 electrolyte and Zn metal surface was 10.60°, significantly lower than that of ZSO electrolyte (72.3°), indicating superior interfacial wettability. This phenomenon can be chiefly attributable to the low dielectric constants of TEP and THF, which reduce the surface tension.

The structure of the TEP-3 electrolyte was further characterized by Fourier-transform infrared spectroscopy (FTIR) and Raman

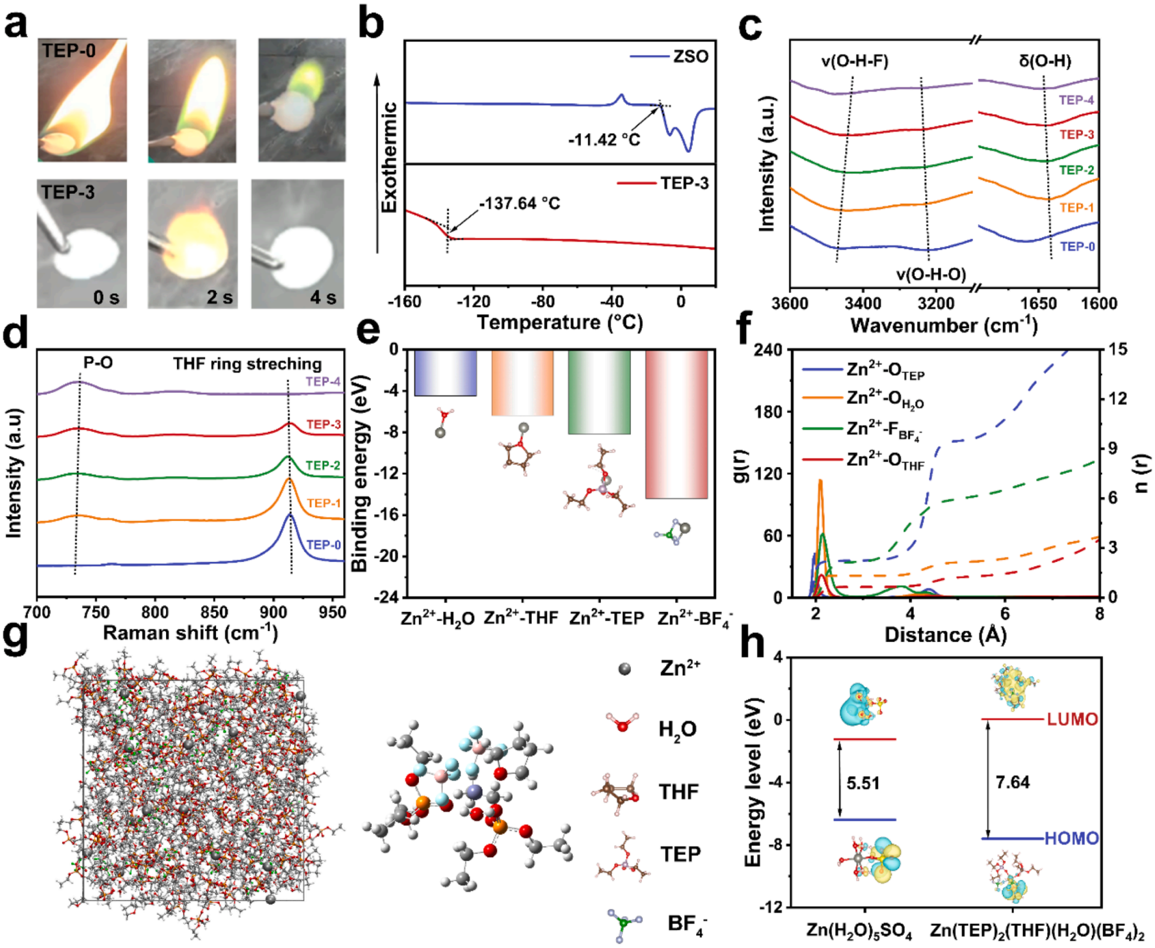

Fig. 2. Electrolyte properties and structure. a) Ignition tests of the separator with TEP-0 and TEP-3 electrolytes. b) Differential scanning calorimetry (DSC) curves of ZSO and TEP-3 electrolytes. c) FTIR spectra of TEP-0, TEP-1, TEP-2, TEP-3, and TEP-4 electrolytes. d) Raman spectra of TEP-0, TEP-1, TEP-2, TEP-3, and TEP-4 electrolytes. e) Binding energies and models of Zn^{2+} with THF, TEP, BF_4^- and H_2O, respectively. f) Radial distribution functions and coordination numbers of Zn^{2+}-O and Zn^{2+}-F. g) A 3D snapshots of TEP-3 and partially enlarged snapshots of the solvated structure of Zn^{2+} derived from MD simulations. h) HOMO/LUMO energy level of $Zn(H_2O)_5SO_4$ and Zn $(TEP)_2(BF_4)_2(THF)(H_2O)$.

spectroscopy. As shown in Fig. 2c, the characteristic peaks observed within the spectral region of 3100–3700 cm^{-1} were representative of the O—H stretching vibrations of H_2O molecules. Specifically, the peaks at around 3470 cm^{-1} and 3214 cm^{-1} were attributed to the interactions between H_2O molecules and BF_4^- ions, as well as solvent molecules, leading to the formation of O—H-F and O—H-O hydrogen bonds, respectively. Notably, the O—H-O bond underwent a blue shift as the TEP concentration increases, indicating that the affinity between H_2O molecules and TEP was stronger than that with THF. Moreover, the O—H bending vibration within the 1600–1700 cm^{-1} shifted to higher wavenumbers also suggested the restructuring of hydrogen bonding, thereby significantly reducing the reactivity of H_2O molecules and suppressing the HER. Furthermore, Raman spectroscopy showed that the characteristic absorption peak of ~734.98 cm^{-1} corresponded to the stretching vibration of the P-O bond within the TEP framework, which exhibited a discernible blueshift. At the same time, the absorption peaks within the range of 860–960 cm^{-1} were attributed to the ring-breathing vibrations of THF, which displayed a tendency to shift towards lower wavenumbers (Fig. 2d). These phenomena confirmed the enhanced interaction between TEP and Zn^{2+}, coupled with a corresponding decrease in the interaction between THF and Zn^{2+}, suggesting that TEP was gradually being integrated into the solvation shell, concurrently leading to a reduction in the coordination number of THF.

Theoretically, the solvation structure of the TEP-3 electrolyte was analyzed using density functional theory (DFT) and molecular dynamics (MD) simulations. As shown in Fig. 2e, the binding energy of Zn^{2+} with H_2O, THF, TEP, and BF_4^- were −4.46 eV, −6.37 eV, −8.17 eV, and −14.41 eV, respectively, showing a preference of Zn^{2+} for binding with anions, facilitating the formation of a H_2O-poor, anion-rich solvation structure. And TEP, THF and BF_4^- exhibited the binding energy of −0.3324 eV, −0.3630 eV and −0.7270 eV with H_2O, respectively, both higher than the binding energy of −0.3308 eV between H_2O (Figure S9). Meanwhile, the binding energy between TEP (with a higher dielectric constant) and water was lower than that between THF and water, which can be attributed to the greater steric hindrance of TEP. Furthermore, NMR spectroscopy was also used to analyze the H_2O activity. As shown in Figure S10, with the introduction of TEP, hydrogen bonds between H_2O molecules were further disrupted, which was consistent with the FTIR results. Molecular dynamics (MD) simulations were also conducted to analyze the solvation structures. As shown in Fig. 2f, the radial distribution functions (RDFs) showed that the average coordination numbers (CN) for Zn-O (TEP), Zn-O (THF), Zn-O (H_2O), and Zn-F(BF_4^-) were 2.23, 0.64, 1.32, and 2.15, respectively, confirming their successful participation in the Zn^{2+} solvation structure and forming a solvation structure of $Zn(TEP)_{2.23}(THF)_{0.64}(H_2O)_{1.32}(BF_4)_{2.15}$ .The 3D snapshot was shown in Fig. 2 g, for the TEP-3 electrolyte, Zn^{2+} coordinated with one H_2O, one THF, two TEP, and two BF_4^-. Such a unique solvation structure will derive a stable SEI enriched with ZnF_2 and $Zn_3(PO_4)_2$ on the surface of Zn metal anode during electrochemical cycling, thereby achieving high interfacial stability and rapid Zn^{2+} transport. However, for the bare $ZnSO_4$ electrolyte system, Zn^{2+} formed a solvation shell with five H_2O molecules and one SO_4^{2-}, with the average CN of 4.95 and 1.06 for Zn-O (H_2O) and Zn-O (SO_4^{2-}) in the solvation shell, respectively (Figure S11). DFT calculation further indicated that the energy gap for $Zn(TEP)_2(BF_4)_2(THF)(H_2O)$ was 7.64 eV, greater than that of $Zn(H_2O)_5SO_4$, showing higher redox stability (Fig. 2h). Accordingly, linear sweep voltammetry (LSV) also indicated that the TEP-3 electrolyte exhibited higher electrochemical stability, and the electrochemical window was significantly broadened to 2.89 V (Figure S12). As shown in Figure S13, the de-solvation energy (E_a) was obtained by the classic Arrhenius equation. Notably, the E_a of the TEP-3 electrolyte (44.27 kJ mol^{-1}) was significantly higher than that of the ZSO electrolyte (30.58 kJ mol^{-1}), suggested that Zn^{2+} required a greater driving force and to higher initial nucleation overpotential to achieve electrochemical deposition, which was beneficial for sTable 3D diffusion process, thereby achieving parallel Zn deposition.

2.2. *Interface and nucleation behavior*

To explore the advancement of such a lean-water solvation structure in suppressing surface corrosion and stabilizing interface, we first evaluated the corrosion behavior of Zn metal anode after immersion. As shown in Fig. 3a, the Zn metal anode exhibited a flat and smooth surface after soaking in the TEP-3 electrolyte for 7 days, in stark contrast to the Zn surface after immersing in ZSO electrolyte, which corresponded a surface adorned with an array of haphazardly arranged, flaky residues (Fig. 3b). Similarly, the SEM images of Zn metal anode after immersing in the TEP-3 electrolyte for 7 days at −20 °C and −40 °C also confirmed the superior corrosion resistance (Figure S14). Additionally, XRD analysis of Zn metal anode after soaking in bare $ZnSO_4$ electrolyte showed an obvious byproduct peak, corresponding to $Zn_4(OH)_6SO_4{\cdot}5H_2O$, whereas no new peaks emerged when using the TEP-3 electrolyte (Figure S15). Furthermore, linear polarization curves were also used to analyze the corrosion behavior. As shown in Fig. 3c, compared to bare ZSO electrolyte, the self-corrosion potential shifted from −0.006 V to −0.001 V when using the TEP-3 electrolyte, and corresponding self-corrosion current was significantly reduced, indicating corrosion inhibition. At the same time, LSV was employed to analyze HER, which was shown in Fig. 3d The hydrogen evolution potential in the TEP-3 electrolyte showed a significantly more negative value compared to bare $ZnSO_4$ electrolyte, corresponding to the inhibited HER.

HOMO and LUMO were also used to analyze the possibility of SEI formation. Generally speaking, a higher HOMO energy level indicated a greater tendency to coordinate with Zn^{2+}. And the HOMO energy levels of THF, TEP, BF_4, and H_2O were −6.66 eV, −7.85 eV, −3.78 eV, and −8.15 eV, respectively (Fig. 3e), indicating that BF_4^- had the strongest coordinating ability with Zn^{2+}, followed by TEP and THF, with H_2O. Meanwhile, upon coordination with Zn^{2+}, compared to the large energy gap between Zn^{2+} and H_2O, the remaining three components displayed narrower energy gaps, enabling rapid electron transition between HOMO and LUMO, suggesting effectively participating in electrochemical reactions and forming SEI layer (Fig. 3f). Subsequently, after cycling 100 cycles, the SEI derived from the solvation structure of $Zn(TEP)_{2.23}(THF)_{0.64}(H_2O)_{1.32}(BF_4)_{2.15}$ was investigated. As shown in Figure S16, EDS mapping revealed a uniform distribution of B, O, F, and P on the Zn surface after cycling, indicating the formation of SEI on the Zn anode. And then, XPS spectra was further used to analyze the composition and structure of SEI layer. As shown in Fig. 3 g, in the F 1 s spectrum, the peak at 685.08 eV was corresponded to ZnF_2. Notably, the ZnF_2 peak remained detectable even with prolonged Ar^+ sputtering, suggesting the formation of a homogeneous ZnF_2 distribution on the Zn anode surface. Additionally, the peak located at 192.28 eV was assigned to B-O, primarily originating from BF_4^- ions in the solvation structure (Figure S17a). Meanwhile, the C 1 s spectrum exhibited the C—C/C—H (284.80 eV) and C—O (287.88 eV) peaks and O 1 s demonstrated the peaks of ZnO (~532.18 eV), demonstrating that both TEP and THF participated in the electrochemical reduction process, forming an organic-inorganic hybrid SEI layer (Figure S17 b&c). Given the participation of TEP in the solvation structure, the P 2p XPS spectrum was further analyzed. As shown in Fig. 3h, the peak at 139.78 eV was identified as $Zn_3(PO_4)_2$, XPS depth profiling confirmed that $Zn_3(PO_4)_2$ was evenly distributed within the SEI layer under varying sputtering durations, which can significantly enhance the Zn^{2+}diffusion kinetics, particularly under low temperature [39] Remarkably, all SEI components maintained uniform distributions with increasing etching depth, indicating the high stability of the SEI layer derived from the TEP-3 electrolyte. Thus, it can be concluded that when using the TEP-3 electrolyte, a stable SEI layer enriched with ZnF_2 and $Zn_3(PO_4)_2$ was derived from the solvation structure of $Zn(TEP)_{2.23}(THF)_{0.64}(H_2O)_{1.32}(BF_4)_{2.15}$, which effectively isolated the Zn metal anode from the electrolyte, preventing side reactions and accelerating Zn^{2+} ion transport. The SEI layer on the surface of the Zn anode after cycling at −40 °C was also characterized. The corresponding elemental mapping indicated that an

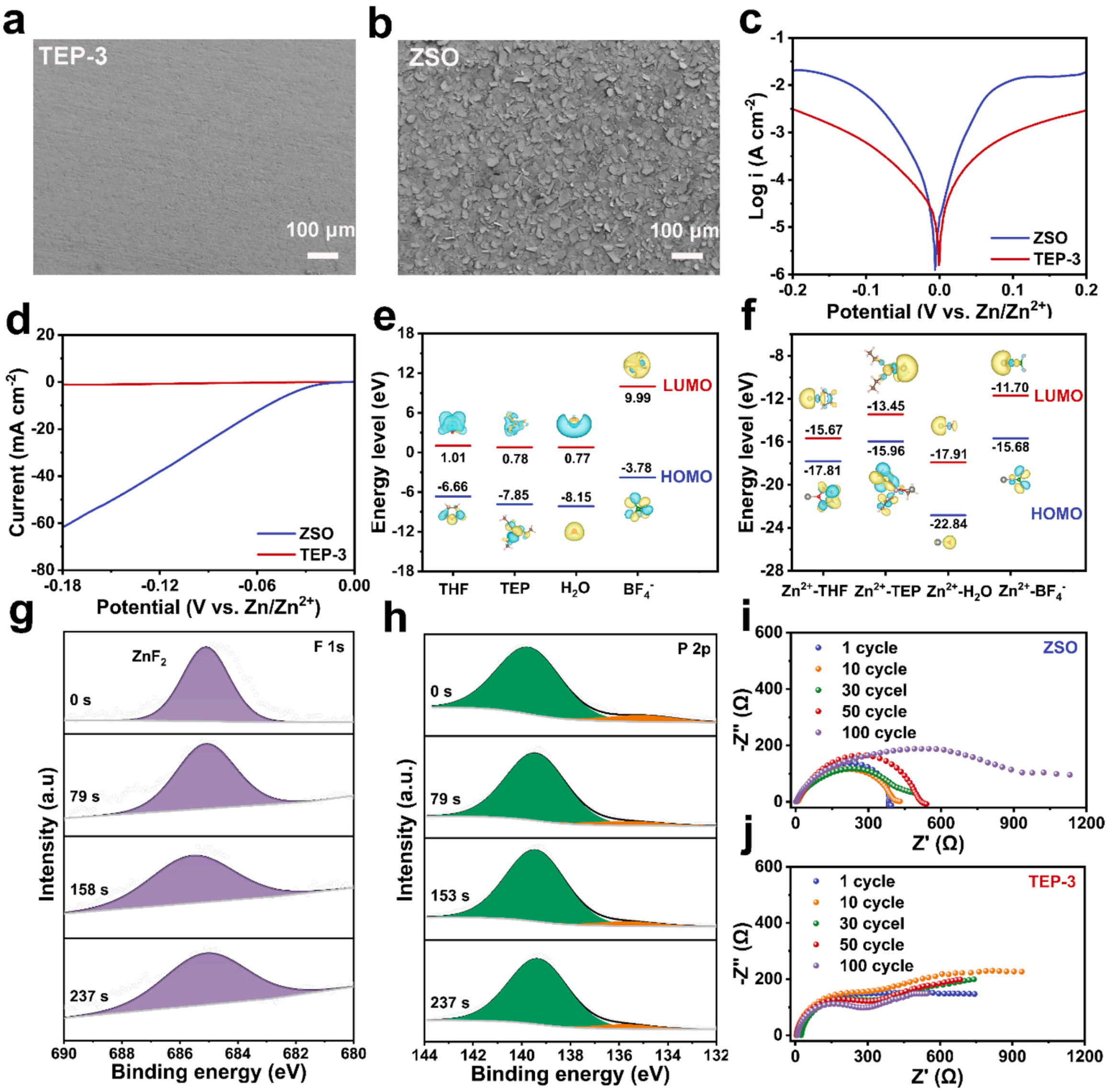

Fig. 3. Interface behavior. a-b) SEM image of Zn foils after 7 days of immersion in ZSO electrolyte a) and TEP-3 electrolyte b). c) Tafel curves of Zn || Zn symmetric cells in ZSO and TEP-3 electrolytes. d) HER curves for Zn electrodes in ZSO and TEP-3 electrolytes. e) HOMO/LUMO energy level of THF, TEP, BF_4^-, and H_2O. f) HOMO/LUMO energy level of Zn^{2+} with THF, TEP, BF_4, and H_2O. g-h) XPS spectral of Zn metal anode cycled in TEP-3 electrolyte with different etching depths. i-j) Electrochemical impedance spectroscopy (EIS) at specific cycle numbers with ZSO electrolytes (i) and TEP-3 electrolytes (j).

SEI layer containing ZnF_2 and $Zn_3(PO_4)_2$ was also formed, which was beneficial for the Zn^{2+} transport at low temperatures (Figure S18). Furthermore, EIS measurement at different cycle numbers revealed that charge transfer resistance (R_{ct}) demonstrated a progressive increase in the ZSO electrolyte with cycling, mainly due to dendritic Zn growth and by-product accumulation (Fig. 3i). In contrast, TEP-3 electrolyte system showed a stable R_{ct}, indicating that the SEI remained stable during cycling (Fig. 3j). The interfacial stability was further verified through a more precise in situ impedance testing. As shown in Figure S19a&b, for the TEP-3 electrolyte systems, during the Zn deposition process, the impedance exhibited a decreasing trend, while that in the ZSO electrolyte displayed an increasing trend. A similar trend was observed during longer-term plating/stripping processes, which may be attributed to the gradual formation of the SEI layer (Figure S19c-d). Furthermore, the DRT profiles revealed two distinct peaks: the first peak corresponds to contact resistance, and the second peak is assigned to SEI layer resistance (R_{SEI}) [39–41] As shown in Figure S20, in the TEP-3 electrolyte systems, it demonstrated significantly lower contact resistance and R_{SEI}, which can be attributed to the less accumulation of by-products, thus ensuring a stable electrode-electrolyte interface. The TEP-3 electrolyte demonstrates significantly lower contact resistance and RSEI compared to other systems. This improvement is primarily attributed to the absence of parasitic byproduct accumulation and the protective nature of the SEI layer, which collectively ensure a stable electrode-electrolyte interface.

Furthermore, the Zn^{2+} nucleation mode and growth behavior were analyzed using chronoamperometry (CA). As shown in Fig. 4a, when the polarization voltage was fixed at −150 mV, the current density in the ZSO electrolyte gradually increased over time, corresponding to a constant 2D diffusion process, which leaded to deposition Zn on existing irregular nuclei to minimize surface energy, ultimately triggering the formation of uncontrollable Zn dendrites. In contrast, in the TEP-3 electrolyte, the response current remained constant, indicating uniform and sTable 3D diffusion, thereby achieving parallel Zn deposition. Correspondingly, the initial nucleation overpotential was also evaluated by Zn | Cu half cells. Compared to the bare ZSO electrolyte, the TEP-3 electrolyte exhibited a higher nucleation overpotential, which had the potential to facilitate the formation of fine and dense grains (Fig. 4b).

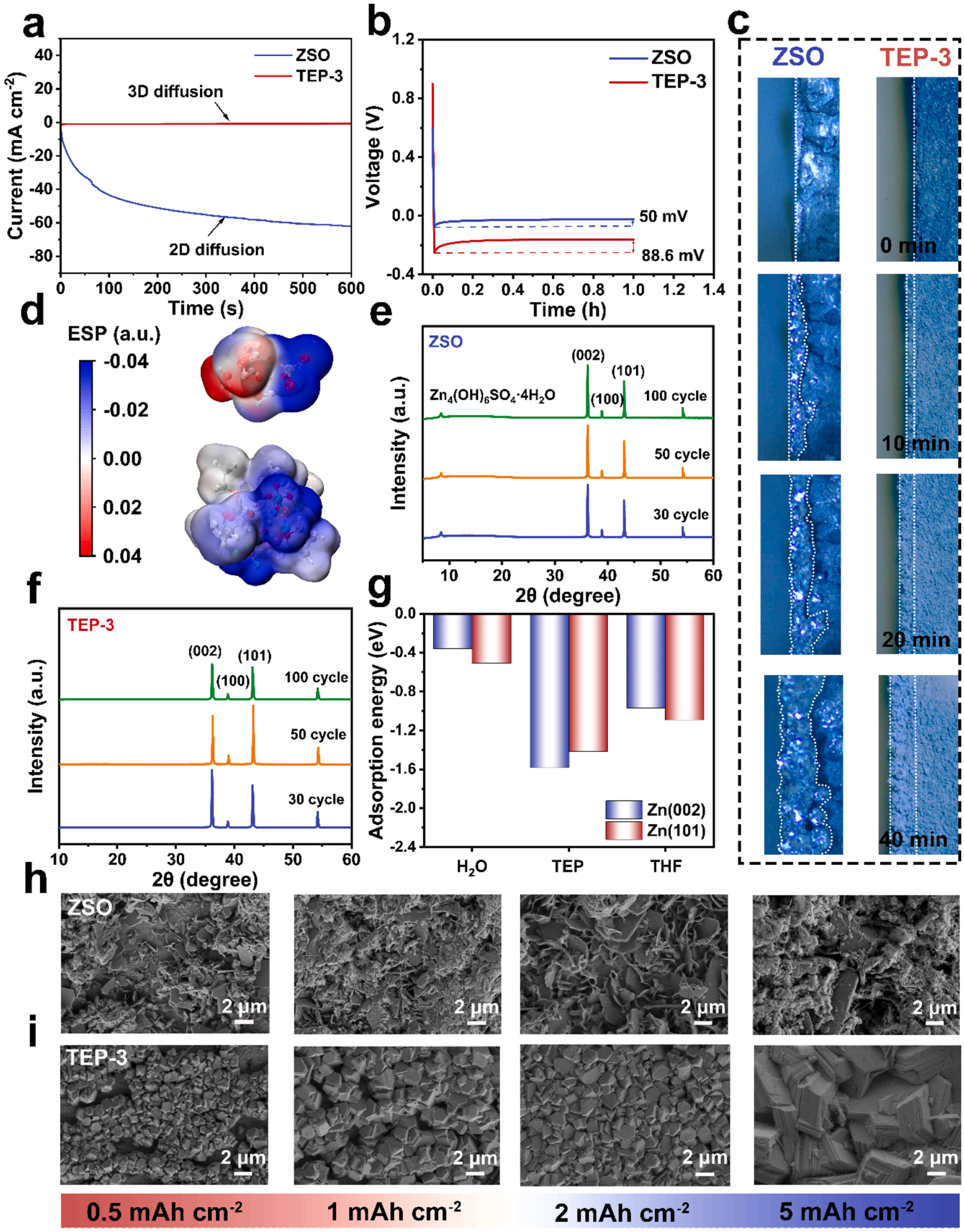

Fig. 4. Zn nucleation behavior. a) Chronoamperometry of Zn electrodes in different electrolytes under a polarization voltage of 0.15 V for 600 s. b) Initial Zn nucleation overpotential of Zn | Cu cells in ZSO and TEP-3 electrolytes at 1 mA cm^{-2}/1 mAh cm^{-2}. c) In situ recording false color images of Zn deposition (0, 10, 20, and 40 min) under ZSO and TEP-3 electrolyte at the current density of 5 mA cm^{-2}. d) Surface electrostatic potentials of $Zn(H_2O)_5SO_4$ and Zn $(TEP)_2(BF_4)_2(THF)(H_2O)$. e-f) XRD patterns of Zn electrodes with different cycles in ZSO electrolyte (e) and TEP-3 electrolyte (f). g) Comparison of the adsorption energies of H_2O, THF and TEP molecules on the Zn(101) and (002) crystal planes. h-i) SEM images of Zn deposition with different capacities in ZSO electrolyte and TEP-3 electrolyte.

Besides, an in-situ optical device was assembled to observe the Zn^{2+} nucleation and growth behavior, which was shown in Fig. 4c. At a current density of 5 mA cm^{-2}, Zn deposition in the TEP-3 electrolyte demonstrated a uniform and dense morphology as the deposition time increased, which can be attributed to the uniform and sTable 3D diffusion behavior. However, when using the bare ZSO electrolyte, an uneven Zn deposition with irregular protrusions was observed, corresponding to the 2D diffusion process. In theory, compared to the solvation structure of $Zn(H_2O)_5SO_4$ in the bare ZSO electrolyte, the solvation structure of Zn $(TEP)_2(BF_4)_2(THF)(H_2O)$ in the TEP-3 electrolyte exhibited a lower surface charge distribution, which reduced the repulsive force during the de-solvation process, facilitating rapid Zn^{2+} diffusion kinetics (Fig. 4d).

2.3. *Cycling stability and electrochemical performance*

To explore the Zn growth and cycling behavior, the Zn metal anode after cycling was analyzed by XRD. As shown in Fig. 4e, when Zn metal anode cycling in the ZSO electrolyte, the XRD pattern exhibited a new peak corresponding to byproducts, and the diffraction intensity increased with the cycling number, suggesting the continuous accumulation of byproducts over time. This was mainly due to uneven zinc deposition and severe interface side reactions, while HER intensified as the cycling number increased, leading to a locally alkaline pH, thereby forming more byproducts. However, when using the TEP-3 electrolyte, there were no obvious by-products on the Zn metal surface as the number of cycles increased, showing superior corrosion resistance (Fig. 4f). Similarly, the Zn metal anode cycling at low temperature also demonstrated similar results and Zn^{2+} preferentially deposited on the (002) and (101) crystal planes (Figure S21). Theoretically, TEP exhibited adsorption energies of −1.42 eV and −1.58 eV on Zn (002) and Zn (101), respectively, which were stronger than those of H_2O and THF (Figure S22 and Fig. 4 g). This promoted a uniform electric field distribution on the Zn metal surface and formed active sites on the Zn surface, guiding the preferential and uniform Zn deposition on (002) and (101) crystal planes, enhancing the de-solvation process. Following closely, the surface morphology of Zn metal anode after cycling was also characterized by SEM. As shown in Figure S23, a uniform deposition morphology was observed when using the TEP-3 electrolyte, while Zn metal anode cycling in the bare ZSO electrolyte had many small protrusions and the Zn deposition was scattered and stacked, means: dendrites accumulated continuously during the plating/stripping process. Similarly, the Zn metal anode after cycling at low temperature also demonstrated similar results, suggesting that the use of TEP-3 electrolyte effectively avoided the exacerbation of dendrite growth at low temperatures and ensured the stable run of the ZIBs. To gain a deeper insight into Zn deposition behavior, SEM was employed to observe morphologies under a current density of 1 mA cm^{-2} with varying areal capacities. Fig. 4h revealed that as the deposition capacity increases, ZSO exhibited a preferential orientation towards flake-like growth, which was more prone to trigger dendrite formation, thereby compromising the cycling lifespan of the battery. Conversely, in the TEP-3

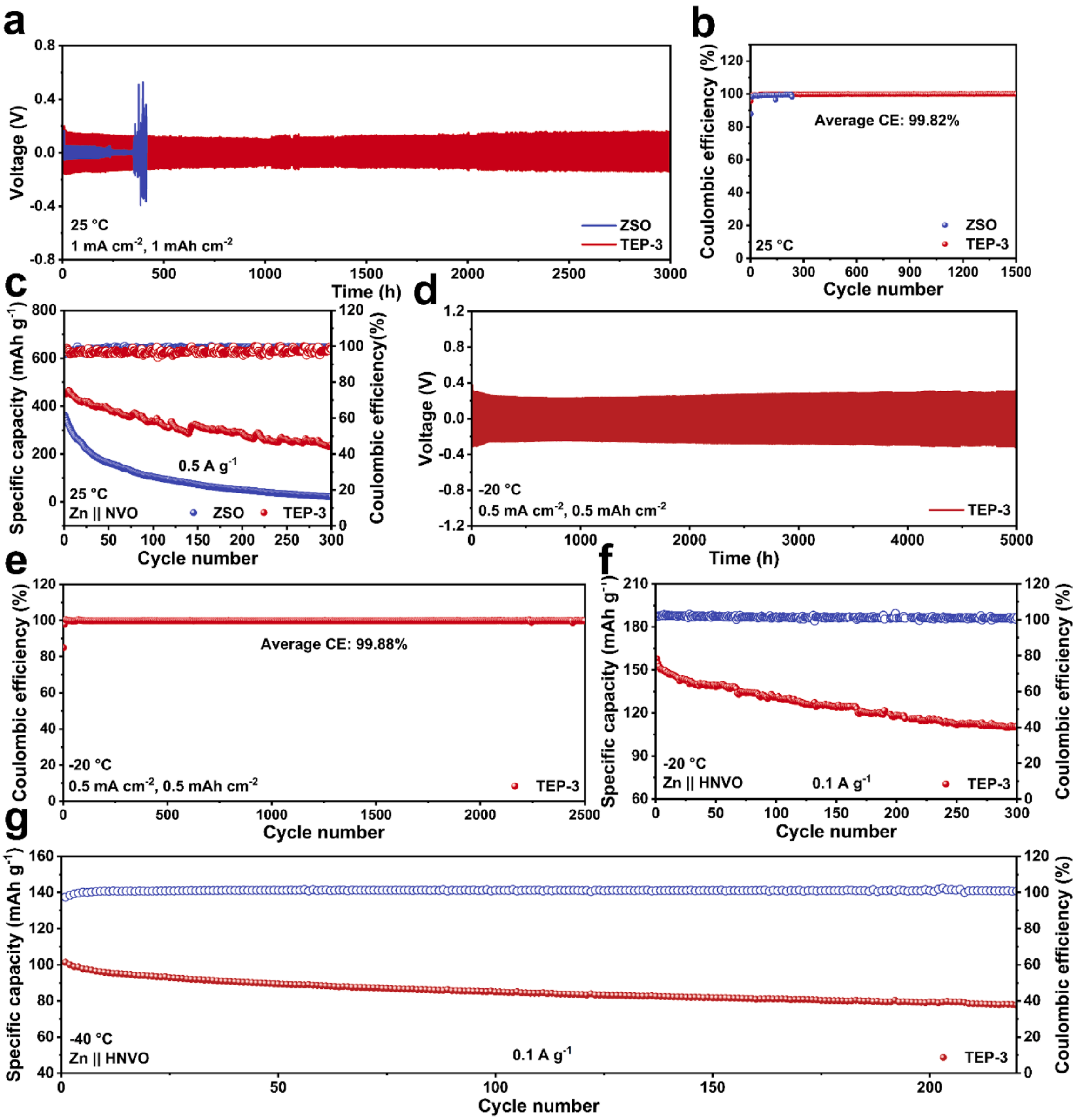

Fig. 5. Electrochemical Performance. a) Cycling performance of Zn || Zn symmetric cells at 1.0 mA cm^{-2}/1.0 mAh cm^{-2} and 25 °C. b) Zn | Cu cells at 25 °C. c) Cycling performance of Zn || NVO full cells at 0.5 A g^{-1} and 25 °C. d) Cycling performance of Zn || Zn symmetric cells at 0.5 mA cm^{-2}/0.5 mAh cm^{-2} and −20 °C. e) Zn | Cu asymmetrical cells at 0.5 mA cm^{-2}/0.5 mAh cm^{-2} and −20 °C. f) Cycling performance of Zn || HNVO full cells at 0.1 A g^{-1} and −20 °C. g) Cycling performance of Zn || HNVO full cells at 0.1 A g^{-1} and −40 °C.

electrolyte, the grains stack in a more uniform and dense manner (Fig. 4i). Notably, at a capacity of 5 mAh cm^{-2}, the grain size increased markedly in both cases, yet the deposition morphology of TEP-3 remained more uniform. Moreover, optical images shown that the Zn deposition on Cu foil after cycling in the TEP-3 electrolyte was more even (Figure S24).

Then, symmetric cells and Zn | Cu half cells were employed to evaluate the cycling stability. As shown in Fig. 5a, the Zn || Zn symmetric cell using the TEP-3 electrolyte exhibited an extended cycling lifespan exceeding 3000 h under 1 mA cm^{-2} and 1 mAh cm^{-2}. In contrast, the cell with the ZSO aqueous electrolyte suffered from severe polarization voltage fluctuations during cycling and failed abruptly after only 500 h, caused by the accumulation of dendrites and severe side reactions during cycling. The Zn | Cu half cells were also assembled to investigate the reversibility of Zn metal anode in different electrolytes. As shown in Fig. 5b, when using the TEP-3 electrolyte, the half cells can maintain a high coulombic efficiency of 99.82 % over 1500 cycles, whereas the CE of Zn | Cu half cells cycled in the bare ZSO electrolyte showed drastic fluctuation and even suddenly dropped after ~230 cycles. Furthermore, we also analyzed the average CE to evaluate the cycling reversibility. As shown in Figure S25, the cells using the TEP-3 electrolyte demonstrated a high average CE of 99.60 %, demonstrating its superior reversibility. Furthermore, under a high discharge capacity (Figure S26), the cells employing the TEP-3 electrolyte demonstrated stable cycling for over 2000 h (~30 % DOD) and 350 h (~60 % DOD), which further proved the unique advantages of TEP-3 electrolyte.

To evaluate the practical application potential, the full cells were assembled using NH_4V_4 O_{10} (NVO) as the cathode. As shown in Fig. 5c and Figure S27, the full cells with the TEP-3 electrolyte delivered a significantly higher discharge specific capacity of 453.33 mAh g^{-1} and low voltage polarization, which can be attributed to the stable electrode-electrolyte interface. Then, the low-temperature electrochemical behavior was also systematically investigated. At −20 °C, the symmetric Zn || Zn cell can run stably over 5000 h at 0.5 mA cm^{-2}/0.5 mAh cm^{-2} with minimal polarization fluctuations (Fig. 5d). Compared to existing studies, this work demonstrated enhanced reversibility under low-concentration and low-temperature condition (Table S3). Even at a higher current density and capacity (1 mA cm^{-2}/5 mAh cm^{-2}), it can also maintain stable cycling for over 900 h (Figure S28), highlighting significantly improved Zn utilization efficiency at low temperatures. At the same time, the Zn | Cu half cells using the TEP-3 electrolyte exhibited remarkable cyclability, showing a high CE of 99.86 % over 2500 cycles at 0.5 mA cm^{-2}/0.5 mAh cm^{-2} (Fig. 5e). These results collectively validate the exceptional interfacial stability and reversibility of the TEP-3 electrolyte at low temperature, positioning it as a promising candidate for practical ZIBs.

Then, the full cells were assembled using $(NH_4)_2V_6O_{16}\cdot 1\cdot 4H_2O$ nanobelts (HNVO) as the cathode material. As shown in Fig. 5f and Figure S29a, the Zn || HNVO full cells delivered an initial discharge specific capacity of 157.79 mAh g^{-1} at 0.1 A g^{-1} with low polarization, retaining high capacity after prolonged cycling. Even at −40 °C, the cells achieved an initial capacity of 101.3 mAh g^{-1} at 0.1 A g^{-1}, maintaining a discharge capacity of 78.02 mAh g^{-1} after 200 cycles, corresponding to a high capacity retention of 77.02 % (Fig. 5 g and Figure S29b). The superior low-temperature electrochemical performance can be attributed to the retained fluidity of electrolyte at low temperatures and stable SEI layer, which synergistically alleviate kinetic barriers. To further evaluate the application potential of the TEP-3 electrolyte, HNVO cathodes with higher mass loading (~4 mg cm^{-2}) were also employed. As shown in Figure S30, the TEP-3 electrolyte still exhibits excellent cycling performance even under such demanding conditions. In all, we have developed a low-concentration and non-flammable electrolyte formula, which has low cost, high safety, excellent physicochemical properties, including but not limited to: ionic conductivity, electrochemical window, etc. showing excellent practical application prospects

3. Conclusion

In summary, we designed a low-concentration and non-flammable electrolyte, which can form a $Zn(TEP)_{2.23}(THF)_{0.64}(H_2O)_{1.32}(BF_4)_{2.15}$ solvation structure, leading to the SEI layer enriched with ZnF_2 and $Zn_3(PO_4)_2$, thus effectively regulating the nucleation and deposition of Zn^{2+}, thereby achieving uniform Zn deposition and rapid Zn^{2+} transport kinetics, especially at low-temperature. Thus, the Zn metal anode can display a high average coulombic efficiency of 99.86 % after 1500 cycles and excellent cycling stability (over 5000 h) at −20 °C, far exceeding that of conventional aqueous electrolytes. Moreover, full cells with the TEP-3 electrolytes show excellent cycling performance from −40 °C to 25 °C. This work offers new insights into designing advanced electrolyte system for ZIBs.

CRediT authorship contribution statement

Rujian Fu: Writing – original draft. **Bo Zhang:** Supervision. **Tiantian Lu:** Data curation. **Chang Liu:** Supervision. **Lifeng Hou:** Writing – review & editing. **Shi Wang:** Writing – review & editing, Supervision. **Yihang Ning:** Funding acquisition. **Zhong Jin:** Writing – review & editing. **Qian Wang:** Writing – review & editing.

Declaration of competing interest

The authors declare that they have no known competing financial interests or personal relationships that could have appeared to influence the work reported in this paper.

Acknowledgements

This work was supported by the National Natural Science Foundation of China (No. 22402146), the Natural Science Foundation of Jiangsu Province (BK20210601), the Beijing Natural Science Foundation-Xiaomi innovation joint Foundation (L223011), Young Elite Scientists Sponsorship Program by CAST (2022QNRC001), Shanxi energy internet research institute (SXEI2023A004), China Postdoctoral Science Foundation (2023M741624), the Project of State Key Laboratory of Organic Electronics and Information Displays, NJUTP (GZR2023010016), Natural Science Foundation of NJUTP (NY223079 and NY224199), Open Research Fund of Guangdong Advanced Carbon Materials Co., Ltd (Kargen-2024B0905 and Kargen-2024B0908), the special fund for Science and Technology Innovation Teams of Shanxi Province (202204051001004).

Supplementary materials

Supplementary material associated with this article can be found, in the online version, at doi:10.1016/j.ensm.2025.104374.

Data availability

Data will be made available on request.

References

[1] L. Yang, Q. Ma, Y. Yin, D. Luo, Y. Shen, H. Dou, N. Zhu, R. Feng, Y. Kong, A. Yu, B. Cheng, X. Wang, Z. Chen, Construction of desolvated ionic COF artificial SEI layer stabilized Zn metal anode by in-situ electrophoretic deposition, Nano Energy 117 (2023) 108799, https://doi.org/10.1016/j.nanoen.2023.108799.

[2] B. Wu, T. Lu, X. Bai, J. Zhang, X. Chang, L. Hou, Y. Wei, Q. Wang, J. Ni, Dual-induced directed deposition mechanism based on anionic surfactants enables long cycle aqueous zinc ion batteries, Small. Methods (2025) 2401838, https://doi.org/10.1002/smtd.202401838.

[3] A. Chen, C. Zhao, J. Gao, Z. Guo, X. Lu, J. Zhang, Z. Liu, M. Wang, N. Liu, L. Fan, Y. Zhang, N. Zhang, Multifunctional SEI-like structure coating stabilizing Zn anodes at a large current and capacity, Energy Environ. Sci. 16 (2023) 275–284, https://doi.org/10.1039/D2EE02931F.

[4] Y. Ma, Q. Ma, Y. Liu, Y. Tan, Y. Zhang, N. Han, S. Bao, J. Song, M. Xu, Multiphilic-Zn group "adhesion" strategy toward highly stable and reversible zinc anodes, Energy Storage Mater. 63 (2023) 103032, https://doi.org/10.1016/j.ensm.2023.103032.

[5] B. Li, B. Zhang, X. Bai, J. Zhang, X. Chang, L. Hou, H. Huang, T. Lu, S. Wang, Z. Jin, Q. Wang, A dynamic self-healing protective layer enabling stable zinc ion batteries through strong Zn-S affinity and intramolecular hydrogen bonding, Angew. Chem. Int. Ed. (2025), https://doi.org/10.1002/anie.202503345.

[6] C. You, R. Wu, X. Yuan, L. Liu, J. Ye, L. Fu, P. Han, Y. Wu, An inexpensive electrolyte with double-site hydrogen bonding and a regulated Zn^{2+} solvation structure for aqueous Zn-ion batteries capable of high-rate and ultra-long low-temperature operation, Energy Environ. Sci. 16 (2023) 5096–5107, https://doi.org/10.1039/D3EE01741A.

[7] K. Liu, Y. Li, T. Zhang, A. Zhu, G. Gan, D. Lin, K. Liu, C. Luan, S. Bu, X. Zhang, Y. Yang, C. Yu, Y. Wu, G. Hong, W. Zhang, Hydrophilic and insulative interface strategy against side reactions for dendrite-free zinc metal anodes, Adv. Funct. Mater. 34 (2024) 2409251, https://doi.org/10.1002/adfm.202409251.

[8] L. Zhang, J. Wu, T. Lu, X. Li, H. Wu, T. Chen, Y. Zhang, J. Wei, M. Hu, X. Zheng, H. Gao, Z.-D. Huang, Q. Wang, S. Wang, Z. Jin, Improving Zn2+ migration via designing multiple zincophilic polymer electrolyte for advanced aqueous zinc ion batteries, Chem. Eng. J. 496 (2024) 153815, https://doi.org/10.1016/j.cej.2024.153815.

[9] K. Liu, M. Sun, Y. Wu, T. Zhang, A. Zhu, S. Bu, C. Luan, K. Liu, Y. Zhou, D. Lin, S. Wu, C.S. Lee, B. Huang, G. Hong, W. Zhang, Binary Electrolyte Additive-Reinforced Interfacial Molecule Adsorption Layer for Ultra-Stable Zinc Metal Anodes, Adv. Mater. (2025) 2420079, https://doi.org/10.1002/adma.202420079.

[10] Y. Meng, M. Wang, J. Wang, X. Huang, X. Zhou, M. Sajid, Z. Xie, R. Luo, Z. Zhu, Z. Zhang, N.A. Khan, Y. Wang, Z. Li, W. Chen, Robust bilayer solid electrolyte interphase for Zn electrode with high utilization and efficiency, Nat. Commun. 15 (2024) 8431, https://doi.org/10.1038/s41467-024-52611-z.

[11] T. Lu, Y. Lin, L. Guan, L. Hou, H. Du, H. Wei, X. Liu, C. Yang, Y. Wei, M. Song, W. Liu, H. Zhou, Q. Wang, Suppressing side reaction and dendritic growth via interfacial cyclization molecule for stable Zn metal anodes, ACS. Appl. Energy Mater. 7 (2024) 61–71, https://doi.org/10.1021/acsaem.3c02209.

[12] C. Cui, D. Han, H. Lu, Z. Li, K. Zhang, B. Zhang, X. Guo, R. Sun, X. Ye, J. Gao, Y. Liu, Y. Guo, R. Meng, C. Wei, L. Yin, F. Kang, Z. Weng, Q.-H. Yang, Breaking Consecutive Hydrogen-Bond Network Toward High-Rate Hydrous Organic Zinc Batteries, Adv. Energy Mater. (2023), https://doi.org/10.1002/aenm.202301466.

[13] T. Wu, C. Hu, Q. Zhang, Z. Yang, G. Jin, Y. Li, Y. Tang, H. Li, H. Wang, Helmholtz Plane Reconfiguration Enables Robust Zinc Metal Anode in Aqueous Zinc-Ion Batteries, Adv. Funct. Mater. (2024) 2315716, https://doi.org/10.1002/adfm.202315716.

[14] Y. Liu, Y. An, L. Wu, J. Sun, F. Xiong, H. Tang, S. Chen, Y. Guo, L. Zhang, Q. An, L. Mai, Interfacial Chemistry Modulation via Amphoteric Glycine for a Highly Reversible Zinc Anode, ACS. Nano 17 (2023) 552–560, https://doi.org/10.1021/acsnano.2c09317.

[15] T. Wang, Q. Xi, Y. Li, H. Fu, Y. Hua, E.G. Shankar, A.K. Kakarla, J.S. Yu, Regulating Dendrite-Free Zinc Deposition by Red Phosphorous-Derived Artificial Protective Layer for Zinc Metal Batteries, Adv. Sci. 9 (2022) 2200155, https://doi.org/10.1002/advs.202200155.

[16] D. Han, C. Cui, K. Zhang, Z. Wang, J. Gao, Y. Guo, Z. Zhang, S. Wu, L. Yin, Z. Weng, F. Kang, Q.-H. Yang, A non-flammable hydrous organic electrolyte for sustainable zinc batteries, Nat. Sustain. 5 (2021) 205–213, https://doi.org/10.1038/s41893-021-00800-9.

[17] F. Bu, Y. Gao, W. Zhao, Q. Cao, Y. Deng, J. Chen, J. Pu, J. Yang, Y. Wang, N. Yang, T. Meng, X. Liu, C. Guan, Bio-inspired trace hydroxyl-rich electrolyte additives for high-rate and stable Zn-Ion batteries at low temperatures, Angew. Chem. Int. Ed. 63 (2024) e202318496, https://doi.org/10.1002/anie.202318496.

[18] Y. Kang, F. Zhang, H. Li, W. Wei, H. Dong, H. Chen, Y. Sang, H. Liu, S. Wang, Modulating the Electrolyte Inner Solvation Structure via Low Polarity Co-solvent for Low-Temperature Aqueous Zinc-Ion Batteries, Energy & Environ Materials (2024) e12707, https://doi.org/10.1002/eem2.12707.

[19] M. Shi, T. Sun, W. Zhang, Q. Nian, Q. Sun, M. Cheng, J. Liang, Z. Tao, Super hydrous solvated structure of chaotropic Ca^{2+} contributes superior anti-freezing aqueous electrolytes and stabilizes the Zn anode, Angew. Chem. Int. Ed. 63 (2024) e202407659, https://doi.org/10.1002/anie.202407659.

[20] Y. Xiong, W. Teng, Z. Zhao, S. Xu, Y. Ma, Y. Gong, D. Li, X. Wang, Y. Shen, Z. Shen, Y. Hu, Effective control of the solution environment in aqueous zinc-ion batteries for promoting (002)-textured zinc growth by a bio-electrolyte additive, Energy Storage Mater. 74 (2025) 103959, https://doi.org/10.1016/j.ensm.2024.103959.

[21] J. Weng, W. Zhu, K. Yu, J. Luo, M. Chen, L. Li, Y. Zhuang, K. Xia, Z. Lu, Y. Hu, C. Yang, M. Wu, Z. Zou, Enhancing Zn-metal anode stability: key effects of electrolyte additives on ion-shield-like electrical double layer and stable solid electrolyte interphase, Adv. Funct. Mater. 34 (2024) 2314347, https://doi.org/10.1002/adfm.202314347.

[22] Z. Zhang, Y. Zhang, M. Ye, Z. Wen, Y. Tang, X. Liu, C.C. Li, Lithium bis(oxalate) borate additive for self-repairing zincophilic solid electrolyte interphases towards ultrahigh-rate and ultra-stable zinc anodes, Angew. Chem. Int. Ed. 62 (2023) e202311032, https://doi.org/10.1002/anie.202311032.

[23] C. Liu, B. Zhang, Z. Liang, X. Bai, J. Zhang, X. Chang, L. Hou, H. Huang, Y. Wei, B. Wu, S. Wang, C. Yang, W. Liu, Q. Wang, Synergistically modulating the inner helmholtz plane and outer helmholtz plane to achieve a stable interface for aqueous zinc ion batteries, Chem. Eng. J. 508 (2025) 160900, https://doi.org/10.1016/j.cej.2025.160900.

[24] B.W. Olbasa, C. Huang, F.W. Fenta, S. Jiang, S.A. Chala, H. Tao, Y. Nikodimos, C. Wang, H. Sheu, Y. Yang, T. Ma, S. Wu, W. Su, H. Dai, B.J. Hwang, Highly reversible Zn metal anode stabilized by dense and anion-derived passivation layer obtained from concentrated hybrid aqueous electrolyte, Adv. Funct. Mater. 32 (2022) 2103959, https://doi.org/10.1002/adfm.202103959.

[25] D. Dong, T. Wang, Y. Sun, J. Fan, Y.-C. Lu, Hydrotropic solubilization of zinc acetates for sustainable aqueous battery electrolytes, Nat. Sustain. 6 (2023) 1474–1484, https://doi.org/10.1038/s41893-023-01172-y.

[26] Q. Zhang, Y. Ma, Y. Lu, L. Li, F. Wan, K. Zhang, J. Chen, Modulating electrolyte structure for ultralow temperature aqueous zinc batteries, Nat. Commun. 11 (2020) 4463, https://doi.org/10.1038/s41467-020-18284-0.

[27] M. Qiu, P. Sun, K. Han, Z. Pang, J. Du, J. Li, J. Chen, Z.L. Wang, W. Mai, Tailoring water structure with high-tetrahedral-entropy for antifreezing electrolytes and energy storage at −80°C, Nat. Commun. 14 (2023) 601, https://doi.org/10.1038/s41467-023-36198-5.

[28] Y. Qiu, X. Zheng, R. Zhang, Q. Lin, M. Li, J. Luo, S. Yang, Z. Liu, Q. Wang, Y. Yu, C. Yang, Boosting zinc-ion batteries with innovative ternary electrolyte for enhanced interfacial electrochemistry and temperature-resilient performance, Adv. Funct. Mater. 34 (2024) 2310825, https://doi.org/10.1002/adfm.202310825.

[29] Z. Zha, D. Li, T. Sun, Q. Sun, J. Hou, Z. Tao, J. Chen, Electrolyte Design via Cation–Anion Association Regulation for High-Rate and Dendrite-Free Zinc Metal Batteries at Low Temperature, J. Am. Chem. Soc. 146 (2024) 31612–31623, https://doi.org/10.1021/jacs.4c09524.

[30] J. Wang, Q. Zhu, F. Li, J. Chen, H. Yuan, Y. Li, P. Hu, M.Sh. Kurbanov, H. Wang, Low-temperature and high-rate Zn metal batteries enabled by mitigating Zn2+ concentration polarization, Chem. Eng. J. 433 (2022) 134589, https://doi.org/10.1016/j.cej.2022.134589.

[31] R. Zhang, W.K. Pang, J.P. Vongsvivut, J.A. Yuwono, G. Li, Y. Lyu, Y. Fan, Y. Zhao, S. Zhang, J. Mao, Q. Cai, S. Liu, Z. Guo, Weakly solvating aqueous-based electrolyte facilitated by a soft co-solvent for extreme temperature operations of zinc-ion batteries, Energy Environ. Sci. 17 (2024) 4569–4581, https://doi.org/10.1039/D4EE00942H.

[32] G. Qu, H. Wei, S. Zhao, Y. Yang, X. Zhang, G. Chen, Z. Liu, H. Li, C. Han, A Temperature Self-Adaptive Electrolyte for Wide-Temperature Aqueous Zinc-Ion Batteries, Adv. Mater. 36 (2024) 2400370, https://doi.org/10.1002/adma.202400370.

[33] Q. Zhang, K. Xia, Y. Ma, Y. Lu, L. Li, J. Liang, S. Chou, J. Chen, Chaotropic Anion and Fast-Kinetics Cathode Enabling Low-Temperature Aqueous Zn Batteries, ACS. Energy Lett. 6 (2021) 2704–2712, https://doi.org/10.1021/acsenergylett.1c01054.

[34] S. Jin Jun, J. Lee, M.-H. Ryu, M. Lee, J. Lee, H. Kim, K. Yim, K.-N. Jung, Electrode interface modulation using 1,3-propane sultone functionalized additives for high-performance Zn-MnO2 aqueous batteries, Chem. Eng. J. 497 (2024) 154394, https://doi.org/10.1016/j.cej.2024.154394.

[35] G. Wang, H. Fu, J. Lu, S. Huang, C. Pei, D. Min, Q. Zhang, H.S. Park, Gradient-Structured and Robust Solid Electrolyte Interphase In Situ Formed by Hydrated Eutectic Electrolytes for High-Performance Zinc Metal Batteries, Adv. Energy Mater. (2024).

[36] D. Han, C. Cui, K. Zhang, Z. Wang, J. Gao, Y. Guo, Z. Zhang, S. Wu, L. Yin, Z. Weng, F. Kang, Q.-H. Yang, A non-flammable hydrous organic electrolyte for sustainable zinc batteries, Nat. Sustain. 5 (2021) 205–213, https://doi.org/10.1038/s41893-021-00800-9.

[37] C. Meng, W.-D. He, H. Tan, X.-L. Wu, H. Liu, J.-J. Wang, A eutectic electrolyte for an ultralong-lived Zn//V_2 O_5 cell: an in situ generated gradient solid-electrolyte interphase, Energy Environ. Sci. 16 (2023) 3587–3599, https://doi.org/10.1039/D3EE01447A.

[38] X. Chen, C. Liu, X. Bai, J. Zhang, X. Chang, L. Hou, H. Huang, Y. Wei, B. Wu, W. Liu, Q. Wang, A thin and homogeneous solid electrolyte interface enriched with ZnF2 and ZnS for highly reversible zinc batteries, Energy Storage Mater. 75 (2025) 103984, https://doi.org/10.1016/j.ensm.2024.103984.

[39] W. Wang, S. Chen, X. Liao, R. Huang, F. Wang, J. Chen, Y. Wang, F. Wang, H. Wang, Regulating interfacial reaction through electrolyte chemistry enables gradient interphase for low-temperature zinc metal batteries, Nat. Commun. 14 (2023) 5443, https://doi.org/10.1038/s41467-023-41276-9.

[40] J. Chen, E. Quattrocchi, F. Ciucci, Y. Chen, Charging processes in lithium-oxygen batteries unraveled through the lens of the distribution of relaxation times, Chem. 9 (2023) 2267–2281, https://doi.org/10.1016/j.chempr.2023.04.022.

[41] D. Li, C. Li, W. Liu, H. Bu, X. Zhang, T. Li, J. Zhang, M. Kong, X. Wang, C. Wang, X. Xu, Constructing a multifunctional SEI layer enhancing kinetics and stabilizing zinc metal anode, Adv. Funct. Mater. 35 (2025) 2415107, https://doi.org/10.1002/adfm.202415107.